

Diverse Metallicities of Fermi Bubble Clouds Indicate Dual Origins in the Disk and Halo

Trisha Ashley¹✉, Andrew J. Fox², Frances H. Cashman¹, Felix J. Lockman³, Rongmon Bordoloi⁴, Edward B. Jenkins⁵, Bart P. Wakker⁶,
Tanveer Karim⁷

¹ Space Telescope Science Institute, 3700 San Martin Drive, Baltimore, MD 21218

² AURA for ESA, Space Telescope Science Institute, 3700 San Martin Drive, Baltimore, MD 21218

³ Green Bank Observatory, P.O. Box 2, Rt. 28/92, Green Bank, WV 24944, USA

⁴ Department of Physics, North Carolina State University, 421 Riddick Hall, Raleigh, NC 27695-8202

⁵ Department of Astrophysical Sciences, Princeton University, Princeton, NJ 08544, USA

⁶ Department of Astronomy, University of Wisconsin-Madison, 475 North Charter Street, Madison, WI 53706, USA

⁷ Center for Astrophysics | Harvard and Smithsonian, 60 Garden Street, Cambridge, MA 02138, USA

Abstract

The Galactic Center is surrounded by two giant plasma lobes known as the Fermi Bubbles, extending ~ 10 kpc both above and below the Galactic plane. Spectroscopic observations of Fermi Bubble directions at radio, ultraviolet, and optical wavelengths have detected multi-phase gas clouds thought to be embedded within the bubbles referred to as Fermi Bubble high-velocity clouds (FB HVCs). While these clouds have kinematics that can be modeled by a biconical nuclear wind launched from the Galactic center, their exact origin is unknown because, until now, there has been little information on their heavy-metal abundance (metallicity). Here we show that FB HVCs have a wide range of metallicities from $< 20\%$ solar to $\sim 320\%$ solar. This result is based on the first metallicity survey of FB HVCs. These metallicities challenge the previously accepted tenet that all FB HVCs are launched from the Galactic center into the Fermi Bubbles with solar or super-solar metallicities. Instead, we suggest that FB HVCs originate in both the Milky Way's disk and halo. As such, some of these clouds may characterize circumgalactic medium that the Fermi Bubbles expand into, rather than material carried outward by the nuclear wind, changing the canonical picture of FB HVCs. More broadly, these results reveal that nuclear outflows from spiral galaxies can operate by sweeping up gas in their halos while simultaneously removing gas from their disks.

Main

Nuclear outflows are an important source of feedback in spiral galaxies. In the Milky Way, evidence of a nuclear outflow is provided by two large plasma bubbles launched from the Galactic center into the halo, known as the Fermi Bubbles. Simulations and observations suggest that the Fermi Bubbles are likely the result of Galactic nuclear activity from Sagittarius A*^[1–4] and that they possibly formed during a Seyfert flare event ~ 3.5 Myr ago that

ionized the Magellanic Stream⁵⁻⁷. However, star formation in the Galactic center cannot be ruled out as a partial contributor to the origin and growth of the bubbles^{8,9}. Their large angular extent ($\pm 55^\circ$ in latitude and $\pm 20^\circ$ in longitude¹⁰⁻¹²) allows us to resolve a nuclear outflow and study its effect on the baryons of a large spiral galaxy in unparalleled detail.

The bubbles have been detected across the electromagnetic spectrum in gamma-rays, microwaves, polarized radio emission, and X-rays^{4,13-15}. Spectroscopic studies in UV metal line absorption, and atomic hydrogen and molecular emission have revealed populations of cool gas clouds embedded within the Bubbles¹⁶⁻²⁴. These Fermi Bubble high-velocity clouds (FB HVCs) are identified by their projected location towards the gamma-ray-defined bubbles and their velocities, which cannot be accounted for by Galactic rotation (typically exceeding absolute velocities of $\sim 90 \text{ km s}^{-1}$). FB HVCs are thought to be associated with the bubbles because their UV-absorption covering fraction (80%) far exceeds that of HVCs directly outside of the Fermi Bubbles that are similarly not co-rotating with the Milky Way disk (28%)^[17].

Previously, all FB HVCs have been assumed to originate in the disk of the Milky Way, becoming entrained in the Fermi Bubbles and traveling to higher Galactic latitudes^{16,17,20}. FB HVCs detected in H I radio surveys are close to the Milky Way disk's central H I cavity²⁵ ($|b| < 10^\circ$) and have kinematics that can be successfully modeled with a biconical outflow. As such, they are thought to originate in the disk of the Milky Way. However, UV-detected FB HVCs seen at Galactic latitudes up to 55° (a projected distance of $\sim 10 \text{ kpc}$ from the disk) are not so clearly connected to the Milky Way disk and have never had their origin confirmed. Simulations have shown that it is difficult to accelerate a cool cloud in a galactic outflow without destroying it²⁶⁻²⁹, as the cloud has to survive the shock and shear of the outflow. Instead, some of the high-latitude UV-detected FB HVCs may be halo clouds that pre-existed the formation of the bubbles.

Metallicity measurements (heavy metal abundances) from H I and UV data can directly

constrain the origin of the FB HVCs, because clouds driven into the bubbles from the Galactic disk are expected to show solar (or super-solar) metallicities, whereas halo clouds should have sub-solar metallicities^{30–32}. We have conducted the first metallicity survey of FB HVCs by combining measurements of three newly-detected FB HVCs with measurements of nine clouds categorized as FB HVCs in the literature^{17,18,20,33}. We calculate new ionization corrections and metallicities for the literature sample in all but one case (see the Methods section for more details). The three newly-detected FB HVCs each have UV spectra from the Cosmic Origins Spectrograph on the Hubble Space Telescope (HST/COS) as well as H I maps and deep single-pointing H I spectra from the Green Bank Telescope (GBT). In Figure 1 we show the location of each sight line on a gamma-ray map of the Fermi Bubbles, including H I maps of the FB HVCs with detected H I emission when available. The H I maps show the environment, morphology, and spatial size of each cloud. The FB HVC toward 1H1613-097 is a centrally concentrated, compact structure ($<0.4^\circ$ in size) while the new FB HVCs, J1919-2958 and J1938-4326 are tenuous and diffuse in H I. These H I maps are used to quantify the effects of beam-smearing on each H I measurement (see the Methods section). We provide a list of each cloud in Table 1 and detailed information for each cloud and sight line in the Methods Section.

Of all the absorption lines covered in the COS dataset (observed with the G130M and G160M gratings), O I $\lambda 1302$ and S II $\lambda 1250$, $\lambda 1253$, $\lambda 1259$ are the most useful for interstellar metallicity measurements because their ionization corrections are small at large H I column densities ($\log N_{\text{HI}} \gtrsim 18.5$ and 19.5 for O I and S II, respectively; N_{HI} in cm^{-2})^{17,34}. Additionally, oxygen does not have large levels of dust depletion and even though sulfur has been shown to sporadically deplete (up to 1 dex in the dustiest clouds)³⁴, sulfur is not typically thought to strongly deplete onto dust³⁵. We therefore use these two ions for metallicity measurements. We have selected our sample to contain all known FB HVCs with detected O I or S II absorption and associated H I detections. Another measurement included in our

sample is a FB HVC toward J1938-4326, which has a C II $\lambda 1334$ detection and an associated H I detection. J1938-4326’s O I absorption is blended with the background quasar’s intrinsic Si III absorption and it has no detected S II absorption. Instead, we use C II $\lambda 1334$ for the metallicity tracer in this cloud as carbon is only weakly depleted³⁴, although the ionization correction is substantial. We also incorporate PKS 2005-489’s metallicity measurement from the literature into the sample³³. Neither O I nor S II detections exist for PKS 2005-489. Instead, its metallicity measurement was made by comparing its H I column and detected ion abundances to those of Milky Way halo gas clouds with measured metallicities; therefore, all ions detected in this sight line were used to determine the FB HVC’s metallicity³³. Additionally, we include FB HVCs with distinct O I detections and H I column density upper limits in our sample, providing lower limit metallicity measurements. We only use O I $\lambda 1302$ detections with H I upper limits because (unlike other elements) oxygen has small ionization corrections for $\log N_{\text{HI}} \gtrsim 18.5$ ^[17]. In Figure 2 we plot the O I or C II absorption profiles and H I single-pointing emission profile for the three newly-detected FB HVCs in our sample.

We find that four FB HVCs in our sample have low metallicities of $\leq 21\%$ solar (one of which is a lower limit), five have metallicities between $\geq 30\%$ and $\geq 59\%$ solar, and three have near solar or supersolar metallicities of $\geq 85\%$ solar (see Table 1). The low metallicities ($\sim 20\%$ solar) are indicative of Galactic halo clouds^{30,31} and are similar to that measured for the X-ray component of the Fermi Bubbles using Suzaku X-ray data³⁶. By comparison, disk clouds that come from the Galactic center should have solar or supersolar metallicities^{37,38}.

Only one of our sight lines, LS 4825, probes the low-latitude portion of the Fermi Bubbles, close to the disk and central H I cavity ($b = -6.63^\circ$) where FB HVCs are expected to have near solar metallicities. LS 4825 has four FB HVCs which have distances between 7 and 21 kpc as evidenced by their absence in absorption spectra toward a closely aligned foreground star¹⁸. We find that the FB HVCs toward LS 4825 (LS 4825-1, -2, -3, -4 at $v_{0\text{UV}} = 92, -78, -205,$ and -155 km s^{-1} , respectively) have metallicities of $\geq 21\%$, $85 \pm_{37}^{41}\% \geq 44\%$, and

≥ 260 % solar. Two of these metallicities are near solar (LS 4825-2 and -4). Of the other two metallicity measurements, LS 4825-1 has an uncertain H I measurement due to a complex H I emission spectrum and potential narrow line O I absorption (see the Methods section for details), and LS 4825-3 has a measurement based on an H I upper limit. Therefore, it is possible that these two FB HVCs have a higher metallicities than reported.

As explained in detail in the Methods section, the metallicity measurements of the new FB HVCs are robust against beam-smearing effects that result from combining pencil-beam UV data with finite-beam radio data. Furthermore, we derive the time-dependent ionization corrections for the FB HVCs and find that a Galactic center Seyfert flare event 3.5 Myr ago does not have a significant effect on the clouds' ionization corrections^{5,6}. Neither of these effects change the result that the FB HVCs have metallicities ranging from $< 20\%$ to 320% solar. These results challenge the previously accepted picture that all FB HVCs were driven out from the Galactic center with solar or even super-solar metallicity.

One potential explanation for the sub-solar metallicities observed in many of the FB HVCs is that the clouds originate in the Milky Way disk with solar metallicity and then become diluted to subsolar metallicities via metal mixing as they travel through the Fermi Bubbles to higher latitudes. However, as we discuss below, we find that metal mixing cannot explain FB HVC metallicities of $Z \lesssim 20\%$ solar. Mixing can occur when cold gas clouds traveling through a hot ambient medium leave a wake of stripped gas behind them. The stripped gas then mixes with the ambient gas reducing its temperature enough to allow for condensation of the hot medium onto the stripped cold cloudlets, resulting in a cloud with a metallicity between the cold cloudlets and hot plasma^{39,40}. In this scenario, FB HVCs originating from Milky Way's disk with solar (or super-solar) metallicity would need to be mixed down to subsolar metallicities ($\leq 20\%$ in some cases) by low-metallicity hot plasma. The metallicity of the Fermi Bubbles' plasma is difficult to determine. The Fermi Bubble X-ray component has a measured metallicity of $\sim 20\%$ solar³⁶; however, these

measurements are based on limited photon statistics and are not necessarily indicative of the metallicity in gamma-ray component of the bubbles. The gamma-ray-emitting plasma is likely enriched with metals from the Milky Way’s ionized interstellar medium and from the shocked hot Milky Way halo component as the bubbles expand into the halo. The interstellar medium has near-solar metallicities and the hot halo has a relatively high metallicity of $\sim 60\%$ solar^{39, 41, 42} so neither source is expected to reduce the Fermi Bubble plasma’s metallicity to $\leq 20\%$ solar. Additionally, current models of cold clouds moving through the Milky Way halo find that it takes tens of Myr for significant portions of the ambient hot halo to condense onto the cloudlets^{43, 44}; this timescale would be even longer in the Fermi Bubbles, which are approximately twice the temperature of the Milky Way halo and therefore take longer to cool and condense³. As such, given that the Fermi Bubbles are only 3-6 Myr old^[1-3, 7], cold cloudlets would not have sufficient time to condense a significant amount of the plasma, leaving them with a relatively unchanged metallicity. Considering all of these effects, we conclude it is unlikely that mixing can explain FB HVCs with $Z \lesssim 20\%$ solar.

We suggest an alternative explanation. FB HVCs have a large range in metallicities because they have two origins: the Milky Way’s disk and its halo. In this picture, one population of FB HVCs is composed of the low-latitude FB HVCs that originate in the disk of the Milky Way and are accelerated away from the Galactic center by the same mechanism that created the Fermi Bubbles. These cool gas clouds could be accelerated by the hot gas flow and eventually become eroded as their mass transfers from a cool to hot phase^{29, 45}. The remnants of many of these clouds likely become too dispersed, ionized, and hot to be seen in the UV as they move to higher latitudes. The second population of FB HVCs is composed of pre-existing halo clouds that are shocked and accelerated as the Fermi Bubbles expand into the halo. As such, they represent the medium into which the Fermi Bubbles expand, rather than material carried out by the Milky Way’s nuclear outflow.

The division between the disk and halo clouds does not occur at a single latitude, as

evidenced by the FB HVC toward M5-ZNG1 (high metallicity at a high latitude of 47°). This outlier suggests that the outflow is complex and that some disk clouds may be able to survive to higher latitudes in the bubbles. While it is not clear how these clouds survive the shock and shear of the Fermi Bubbles, a range of ideas have been suggested from internal magnetic fields suppressing the destruction of the clouds to radiative cooling increasing a cloud's lifetime in a hot outflow^{26–29}. In any case, the UV-detected FB HVCs reported in this paper have a large range of metallicities from $< 20\%$ solar to 320% solar, a result that requires a revision to the canonical picture of FB HVCs and indicates that biconical outflow models need to be refined to account for the clouds' dual origins.

Our new results on the metallicity and origin of FB HVCs reveal the properties of a nuclear outflow in more detail than is possible in any other spiral galaxy. As such, the Fermi Bubbles serve as an important analog for extragalactic nuclear outflows, which can typically only be studied with one-dimensional down-the-barrel pointings. In general, galactic outflows and outward-moving shocks are thought to prevent inflowing cool gas clouds from reaching the disk of a galaxy, thus quenching the star-formation process⁴⁶. While the Fermi Bubbles are not likely strong enough to quench the Milky Way^{47,48}, they remain important for understanding how nuclear outflows entrain and sweep up cool halo gas, thus circulating matter between the disk and halos of galaxies.

Figures

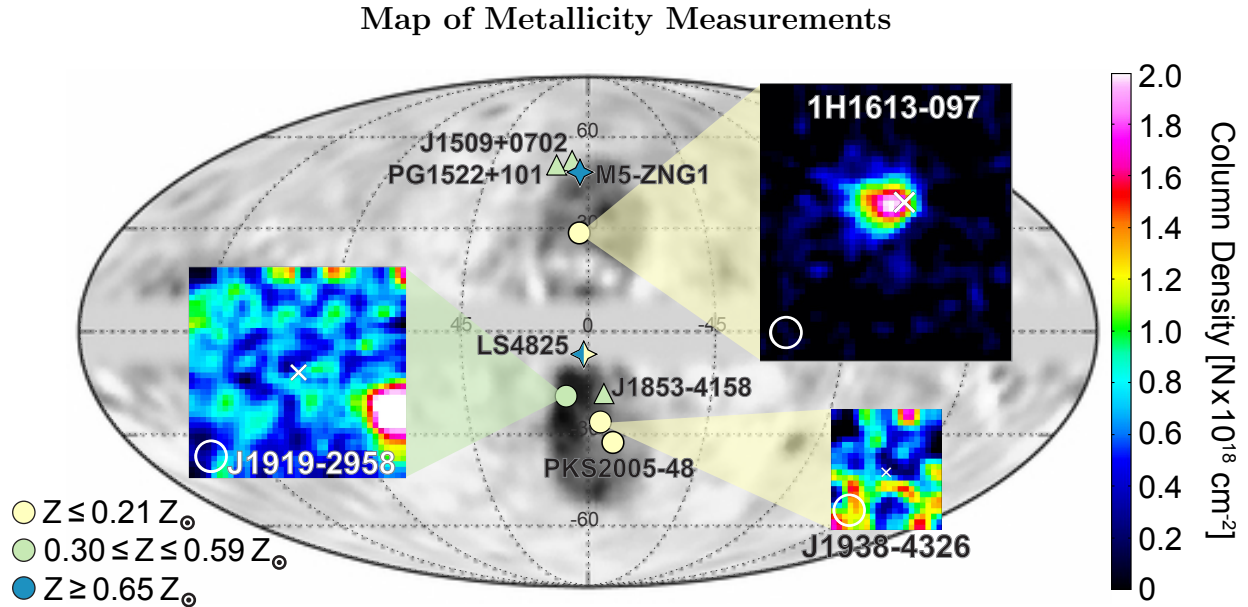


Figure 1: Map of the Fermi Bubbles with UV sight lines from this sample plotted on top of an adapted 3–10 GeV residual intensity Fermi gamma-ray map¹² (grayscale is -5 to $10 \times 10^7 \text{ GeV cm}^{-2} \text{ s}^{-1} \text{ sr}^{-1}$). Yellow, green, and blue symbols correspond to clouds with metallicities of $\leq 21\%$, $30\% \leq Z \leq 59\%$, and $\geq 65\%$ solar, respectively. Circles represent background quasars, stars represent background stellar sight lines, and triangles represent lower-limit metallicity measurements from background quasars. We include the GBT H I maps (when available) plotted to approximately the same angular scale for the sight lines. The circles in the bottom left of each subpanel indicate the 21 cm beam size and the white “X” indicates the location of the UV sight line. The colorscale used for the H I maps represents the H I column densities. The maps were made by integrating over velocities of -201 to -150 km s^{-1} for 1H1613-097, -123 to -56 km s^{-1} for J1938-4326, and 65 to 131 km s^{-1} for J1919-2958. The column colorbar units are in $N \times 10^{18} \text{ cm}^{-2}$ where $N = 1, 3,$ and 5 for 1H1613-097, J1938-4326, and J1919-2958, respectively.

UV Absorption and HI Emission Profiles Used for Metallicity Measurements

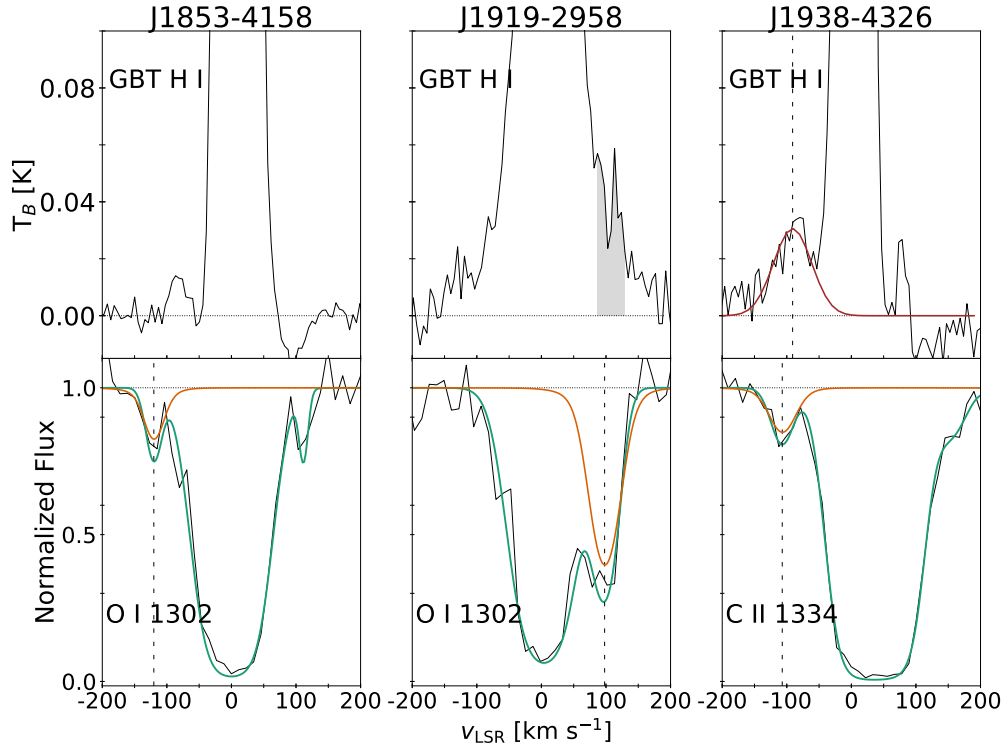


Figure 2: H I emission-line and UV absorption-line profiles used to calculate metallicities for each new sight line. Voigt fits to the UV components of each FB HVC are plotted on top of the data in orange. The full fit to all UV absorption components is plotted in green²⁰. No H I emission associated with J1853-4158’s FB HVC was detected at the sensitivity of the data. J1919-2958’s H I column limits were computed using the velocity range indicated by the grey shaded region after flipping the spectrum around its peak emission and subtracting the resulting spectrum from the original, as discussed in detail in the Methods section. J1938-4326’s Gaussian fit to the FB HVC H I emission is indicated by a red line.

Tables

Table 1: **Sample and Metallicity Measurements**

Reference	Sight line	l ($^{\circ}$)	b ($^{\circ}$)	Spectral Type	X^i	$v_{0\text{UV}}$ (km s^{-1})	Z (Z_{\odot})
UV and H I detections							
TW	J1919-2958	8.18	-18.77	Quasar	O I	97.8 ± 7.7	[0.30, 0.54]
TW	J1938-4326	355.47	-26.41	Quasar	C II	-107.1 ± 8.2	[0.010, 0.10]
17	1H1613-097	3.53	28.46	Quasar	O I	-163 ± 1	0.19 ± 0.10
18	LS 4825-1	1.67	-6.63	B1 Ib-II	O I	92.1 ± 0.8	≥ 0.21
18	LS 4825-2	1.67	-6.63	B1 Ib-II	S II	-78 ± 1	$0.85^{+0.41}_{-0.37}$
49	M5-ZNG1	3.86	46.79	sdO	O I	-124 ± 7	3.2 ± 0.8
33	PKS 2005-489	350.37	-32.60	Quasar	...	168 ± 10	≤ 0.20
UV detections and H I limits							
TW	J1853-4158	354.36	-18.04	Quasar	O I	-120.2 ± 8.4	≥ 0.59
17	J1509-0702	7.80	51.61	Quasar	O I	-115.2 ± 7.8	≥ 0.59
18	LS 4825-3	1.67	-6.63	B1 Ib-II	O I	-205 ± 2	≥ 0.44
18	LS 4825-4	1.67	-6.63	B1 Ib-II	O I	-155 ± 1	≥ 2.6
17	PG 1522+101	14.89	50.12	Quasar	O I	-99.8 ± 8.3	≥ 0.30

The references give the source for the UV and H I measurements (TW=This Work). The Galactic latitude and longitude are given as l and b , respectively. The type of each background source is listed as quasar or the stellar spectral type. X^i represents the ion used for metallicity calculations. The UV Voigt fit local standard of rest (LSR) velocity centroid is $v_{0\text{UV}}$. Z represents the corrected elemental abundances in linear form (for further details on Z calculations, see the Methods Section and Extended Data Fig. 1). J1919-2958’s metallicity is represented by a range due to stray radiation effects (see the Methods section for details). LS 4825 has four detected clouds, listed separately. The M5-ZNG1’s measurement applies to two absorption components that are blended in H I. We treat them as a single cloud because only an average metallicity measurement is possible. PKS 2005-489’s metallicity measurement is a literature measurement made by comparing UV ion and Lyman measurements to other Milky Way HVCs³³. J1938-4326’s metallicity limit includes an estimate for dust depletion and is a range due to multiple H I measurements, as explained in detail in Supplementary Information Section 1.

Methods

Sample

Our full sample consists of nine sight lines passing through or near the Fermi Bubbles. Three of the nine sight lines are new quasar sight lines²⁰ and the other six are taken from the literature^{17,18,33,49}. We have UV O I or S II absorption and H I emission measurements for five FB HVCs. We also have O I absorption measurements and measure the H I limits for five more FB HVCs. Additionally, we have one FB HVC with C II absorption and H I emission measurements and another FB HVC with a UV-based literature metallicity measurement. The UV data for all nine sight lines has been previously calibrated and analyzed^{17,18,20,33,49}. We make new measurements for the UV absorption or H I emission associated with three literature FB HVCs (J1509-0702, PG 1522+101, and LS 4825; see the “UV Ion and H I Column Densities of the Literature Sample” section below). Most of the FB HVC’s in our sample have not had their metallicities previously calculated and many of the metallicity calculations in the literature do not include an ionization correction, an important correction for these clouds that are exposed to the Galactic, extragalactic, and Seyfert flare ionizing radiation fields, in addition to cosmic rays. Table 1 lists information for each sight line and associated cloud(s). The names of several of the targets are abbreviated throughout the paper as follows: J1853-4158=UVQS J185302.65-415839.6, J1919-2958=UVQS J191928.05-295808.0, J1938-4326=UVQS J193819.59-432646.3, and J1509-0702= SDSS J150928.29+070235.8.

Observations and Data Reduction for Three New Sight Lines

The three new targets were selected from the UV-bright QSO Survey (UVQS) catalog⁵⁰ and were observed under HST Program ID 15339 (PI: A. Fox) and GBT Programs GBT18A-221 (PI: A. Fox) and GBT20B-444 (PI: T. Ashley). For each new sight line we obtained both GBT single-pointing spectra and GBT H I maps. The single-pointing spectra were used for

metallicity measurements and the maps were used for beam-smearing calculations and to ascertain the FB HVCs' gaseous environments.

The Voigt fit parameters of the new FB HVCs' UV ions used for metallicity measurements are listed in Extended Data Fig. 2. We note that the FB HVC toward J1919-2958 may be composed of two strongly blended absorption features separated by $\lesssim 20 \text{ km s}^{-1}$, the spectral resolution of COS. Without clearly separated components in any other UV-detected ions²⁰ we are unable to confirm that there are two absorption features contributing to the FB HVC. Therefore, we treat the absorption and emission associated with the FB HVC as one cloud.

The GBT single-pointing H I spectra were calibrated using standard techniques⁵¹. This includes a correction for stray radiation, defined as any 21-cm H I emission that enters the receiver through the telescope's sidelobes, rather than via the main beam. This complicates our derivation of an accurate N_{HI} for J1919-2958, where a GBT sidelobe lies near the Galactic plane, picking up stray emission at $v_{\text{LSR}} < 125 \text{ km s}^{-1}$ for most of the time when this quasar is observable from Green Bank. For J1919-2958, stray radiation dominates the detected signal over the velocity range of the UV absorption and the standard correction technique yields highly uncertain, and in some cases unphysical results. Because stray radiation must always have a positive amplitude, for J1919-2958 we use the scans with minimum H I emission in the uncorrected data to derive a strict upper limit and a range on the possible values of the H I column density.

Toward J1938-4326 the entire observed HI spectrum was decomposed into Gaussian components using the minimum number of components needed to obtain a fit with low residuals. The resulting Gaussian fit parameters are listed in Extended Data Fig. 2.

We were unable to fit accurate Gaussian components to J1919-2958's H I spectrum due to strong blending with the Milky Way's H I emission. To measure J1919-2958's H I column densities, we assume that the Milky Way disk's H I emission has symmetric positive and negative velocity wings and there is only one FB HVC along the line of sight. The H I

spectrum is inverted along its velocity axis about the velocity of the peak intensity (close to zero) and subtracted from the original spectrum. The remaining “flipped-and-subtracted” spectrum is shown in Extended Data Fig. 3. We then integrate the remaining emission with a velocity near that of the UV-detected FB HVC velocity range ($v_{0\text{UV}} = 97.8 \pm 7.7 \text{ km s}^{-1}$, $b = 25.9 \pm 2.5 \text{ km s}^{-1}$) and calculate $\log N_{\text{HI}}$ using Equation 1. For this method, we use two velocity ranges for J1919-2958’s H I integration: $82.7 - 133.4 \text{ km s}^{-1}$ and $107.0 - 133.4 \text{ km s}^{-1}$. The velocity ranges were chosen to include both or one of the apparent H I Gaussian-like features in the “flipped-and-subtracted” spectrum near the velocity range of the O I absorption feature (see Extended Data Fig. 3). The larger range is inclusive of all potential emission associated with the FB HVC and the stray radiation, making the column density an upper limit, while the smaller range excludes any emission that likely contains strong stray radiation, providing a lower limit for the H I column density. We calculate the error on the area as the average root-mean-square (rms) of the noise (0.024 K; measured from emission-free channels) times the channel width and the square root of the number of channels.

The H I column density for J1919-2958 and 1938-4326 was calculated using the standard relation:

$$N_{\text{HI}}[\text{cm}^{-2}] = 1.823 * 10^{18} \int T_B(v) dv [\text{K km s}^{-1}] \quad (1)$$

where $T_B(v)$ is the velocity-dependent brightness temperature. For the Gaussian fit to J1938-4326’s FB HVC, the integral reduces to $\int T_B(v) dv [\text{K km s}^{-1}] = 1.064 h \text{ FWHM} [\text{K km s}^{-1}]$, where h is the height of the Gaussian and FWHM is the full width of the Gaussian at half maximum. A check on J1938-4326’s H I column density measurement is conducted in Supplementary Information Section 2 using the flip-and-subtract method described above. For J1853-4158, we calculate the H I column upper limit as that which is given by three times the rms over the detected O I’s FWHM:

$$N_{\text{HI}} \leq 3 \cdot 1.823 \cdot 10^{18} \text{ rms } \Delta v \sqrt{n}, \quad (2)$$

where Δv is the channel width in km s^{-1} , and n is the number of H I spectrum channels in the velocity range of the detected O I's FWHM. The H I column densities for the three new FB HVCs are listed in Extended Data Fig. 2.

GBT H I 21 cm emission maps around the central quasars were obtained in addition to single-pointing spectra for the three new sight lines. These frequency-switched data were calibrated using standard techniques, smoothed to $\sim 3 \text{ km s}^{-1}$, and corrected for stray radiation⁵¹. All data from the XX polarization in the GBT maps are discarded due to spurious spectral features, as discussed in the Supplementary Information Section 3 (see also Supplementary Figure 1).

We present the GBT H I moment zero map for J1919-2958 and J1938-4326 in Figure 1 (approximately $1.0^\circ \times 1.0^\circ$ for J1919-2958 and $0.5^\circ \times 0.5^\circ$ for J1938-4326). We do not include J1853-4158's H I map because its single-pointing spectrum does not show an H I detection. We also include in Figure 1 a deep GBT H I map of the 1H1613-097 field that was obtained under GBT programs GBT20A-253 and GBT17B-015 ($\sim 1.2^\circ$ in width). These maps were created by visually inspecting the spectrum extracted from the data cube integrated over one beam around the sight line (using the H I single-pointing detections as a guide). We then integrate channels with potential H I emission from the cloud of interest (velocities of 65 to 131 km s^{-1} for J1919-2958, -123 to -56 km s^{-1} for J1938-4326, and -201 to -150 km s^{-1} for 1H1613-097).

Beam-Smearing Analysis

We use the new FB HVCs' GBT H I maps to investigate small-scale structure by quantifying the level by which beam-smearing affects our measurements. Since we also have 1H1613-097's

GBT map, we included it in our beam-smearing analysis. To quantify beam-smearing effects, we extract spectra from the GBT maps within four equally-spaced beam-sized pointings, each centered a half beamwidth away from the central quasar sight line, and one pointing centered on the sight line itself. We perform a boxcar smoothing of each spectrum by three channels and fit Gaussians to each FB HVC. We then calculate each cloud’s $\log N_{\text{HI}}$ in each pointing and take the largest difference between $\log N_{\text{HI}}$ from the central pointing and the four surrounding pointings as a beam smearing error, ϵ_{Beam} . We compile the beam smearing errors and standard deviation of both the H I velocity centroids and FWHM of fits in Supplementary Table 1. The beam-smearing errors are added to the H I column-density errors in quadrature when calculating the metallicity of each cloud. We note that due to the stray radiation problems discussed above in the Observations and Data Reduction section, J1919-2958’s beam smearing error could be affected by stray radiation. However, the resulting ϵ_{Beam} of 0.10 dex is comparable to other beam-smearing error estimates on these angular scales in the literature⁵².

The other literature sight lines either do not have H I emission maps available (LS 4825, J1509-0702, and PG 1522+101) or have their H I columns measured using Lyman lines from FUSE data with an infinitesimal beamsize (M5-ZNG1 and PKS 2005-489). For LS 4825’s H I measurements, we add in quadrature an assumed beam-smearing error of 0.15 dex to H I columns in metallicity calculations, a reasonable assumption for GBT and HST UV derived metallicities^{17,18}.

UV Ion and H I Column Densities of the Literature Sample

For each cloud in the literature sample we use their respective UV ion and H I column densities given in each reference, with the exception of LS 4825-1/2, J1509-0702, and PG 1522+101. We have listed the UV and H I fit parameters used for metallicity measurements for the literature sample in Extended Data Fig. 4.

LS 4825-1 has overlapping narrow and wide O I components reported in the literature at 90.9 and 93.3 km s⁻¹ [18]. In order to obtain a metallicity for LS 4825-1, we add the columns of both components and use their average $v_{0\text{UV}}$ and larger b-value of the two throughout the paper. We also use VPFIT to recalculate the O I columns for two sources with apparent optical depth measurements in the literature from strongly blended absorption, J1509-0702 and PG 1522+101. For all other literature sources, we use the reported UV ion column densities. For M5-ZNG1 and 1H1613-097, we also use the literature reported H I column densities.

For the FB HVC's with H I limits, we calculate the H I column upper limit from GBT (J1853-4158; LS 4825-3/4), LAB⁵³ (J1509-0702), or Green Bank 140' (PG 1522+101) spectra. The H I column upper limit is calculated two ways: using Equation 2 with the rms and using Equation 1 with three times the H I emission integrated over the velocity range of the respective O I absorption's FWHM. From both these methods, the higher column density is used as a conservative H I upper limit.

LS 4825's H I spectra has strongly blended multi-component positive and negative velocity emission, making it difficult to fit a unique set of Gaussians to the spectrum. Additionally, the negative velocity H I component between -110 and -40 km s⁻¹ is reported to have one strong emission peak centered at -70.3 km s⁻¹ and one weak emission peak centered at -88.6 km s⁻¹. However, Mg I and C I, both of which trace cool gas, have absorption components of nearly equal magnitude at similar negative velocities (see Extended Data Fig. 5)¹⁸. Since LS 4825's spectrum is so complex, we have decided to re-measure the H I emission for the FB HVCs.

For LS 4825's negative velocity FB HVC component, we estimate the low-velocity Milky Way H I component's contribution to the negative high-velocity components by using HD 167402's H I spectrum as a "foreground" emission model. We first decompose HD 167402's full H I spectrum into Gaussians with minimum residuals. Then, using these Gaussians as a

model, we remove HD 167402’s negative-velocity emission peaks that are not likely associated with the low-velocity Milky Way H I component (v_{0HI} of -51.5 and -73.9 km s $^{-1}$, FWHM of 18.8 and 45.9 km s $^{-1}$, and peak amplitudes of 0.17 and 0.10 K, respectively; see Extended Data Fig. 5). HD 167402’s residual low-velocity Milky Way H I emission has a slope that matches that of LS 4825’s at negative velocities with only small variations, indicating that HD 167402’s residual emission is a suitable model for LS 4825’s low-velocity H I emission at negative velocities. We subtract HD 167402’s residual H I spectrum from LS 4825’s and fit LS 4825’s remaining negative-velocity H I components with Gaussians using the UV absorption components as a guide and the minimum number of components needed to obtain a low-residual fit. The fit was accomplished with two Gaussians of nearly equal strength, matching the Mg I and C I absorption trends (see Extended Data Fig. 5). We assume the -85.8 ± 1.7 km s $^{-1}$ H I component is associated with the -78 ± 1 km s $^{-1}$ S II absorption because of their adjacent velocities. While UV absorption and H I emission lines from the same cloud should have approximately aligned velocity centroids, the size difference between the GBT 9.1’ beam and the *HST*/STIS pencil beam could lead to different spatial coverage of a cloud with internal velocity structure, and therefore misaligned velocity centroids in the spectra.

The positive velocity Milky Way emission for HD 167402 and LS 4825 are significantly different; therefore, this method only works for negative velocity clouds. For the positive velocity FB HVC, we chose to integrate the H I emission within the O I absorption’s FWHM of 19.8 km s $^{-1}$ and velocity centroid of 92.1 ± 0.8 km s $^{-1}$.

Metallicity Measurements

We calculate the metallicities from the ion abundances $[X^i/\text{H}]$ as:

$$\left[\frac{\text{X}}{\text{H}}\right] = \left[\frac{\text{X}^i}{\text{H}}\right] + IC(\text{X}),$$

where $\left[\frac{\text{X}^i}{\text{H}}\right] = \log\left(\frac{N_{\text{X}^i}}{N_{\text{H I}}}\right) - \log\left(\frac{\text{X}}{\text{H}}\right)_{\odot}$

(3)

where X is the element under study, X^i is the observed ion of that element, IC is the ionization correction, N_{X^i} and $N_{\text{H I}}$ are the ionic and atomic hydrogen column densities, respectively, and $\log(\text{X}/\text{H})_{\odot}$ is the solar abundance of that element⁵⁴. The ionization corrections are important for FB HVCs given their location close to the Galactic center and within the cone of a potential past Seyfert flare^{5,6} exposes them to intense radiation fields. Furthermore, their low $N(\text{H I})$ values are indicative of high levels of ionization.

We derive the ionization corrections for the new FB HVCs by performing a suite of photoionization models using CLOUDY v.17.02⁵⁵. The CLOUDY models are calculated for both an equilibrium case and a time-dependent case to explore the effects of a potential Seyfert flare^{5,6} on the ionization corrections. Since J1919-2958 has two H I column densities, we have run two sets of CLOUDY models for this cloud; these models are compared in the Supplementary Information Section 4. To increase our sample for the time-dependent models, we also include the FB HVC towards 1H1613-097¹⁷. We discuss the ionization corrections for the rest of the sample below.

Equilibrium Models

We first model the time-independent ICs for an ionization equilibrium state in CLOUDY. Physically these models describe the steady-state ionization conditions of clouds existing in the halo before a Seyfert flash event. These models are used as input parameters for the time-dependent models and are later used to confirm whether the time-dependent models strongly affect the present-day ionization corrections.

We adopt a plane-parallel geometry with a slab of uniform density illuminated on both sides by a position-dependent combined Galactic and extragalactic radiation field^{56–58}. The field has a normalization scaled to a distance of 10 kpc along the northern Fermi Bubble line of sight to 1H1613-097¹⁷. This field is also suitable for J1919-2958 and J1938-4326 given that the radiation field models are comparatively symmetric up to 10 kpc⁵⁸, as well as the similar absolute latitude of 1H1613-097 ($b = 28.5^\circ$) with J1919-2958 ($b = -18.77^\circ$) and J1938-4326 ($b = -26.41^\circ$). Additionally, we include the cosmic ray background in our radiation field⁵⁹.

For each FB HVC, we construct a grid of CLOUDY models over a range of hydrogen number densities ($\log n_{\text{H}}$) between -2 and 1 in 0.5 dex intervals, with the metallicity fixed to the ion abundance values presented in Extended Data Fig. 1. The model for each cloud was run until their respective measured H I column densities were reached. The value of $\log n_{\text{H}}$ was determined by comparing the observed column density ratio [Si III/Si II] to the model-inferred ratio at each step in the grid of hydrogen densities, and interpolating to find the best match (see Supplementary Fig. 2 for the observed Si II and Si III absorption profiles). Si II absorption associated with J1938-4326’s FB HVC was not detected. We instead use the Si III/C II ratio assuming that both ions have the same abundance relative to solar. Once a value for $\log n_{\text{H}}$ was determined for each FB HVC, the model was run again for that specific value in order to obtain exact model results.

Non-Equilibrium Time-dependent Models

There is the strong evidence that a ~ 3.5 Myr old Seyfert flare from the Galactic center impacted the Magellanic Stream and resulted in enhanced present-day $\text{H}\alpha$ emission and UV ionization levels in the stream^{5–7}. Since the FB HVCs are approximately ten times closer to the Galactic center than the Magellanic Stream, there may also be enduring ionization effects from the Seyfert flare on the FB HVCs. We use CLOUDY to follow the evolution of the FB HVCs near a time-variable incident radiation field. In this time-dependent non-equilibrium

model, ionization and recombination are not in balance and thus a net rate of change for an ion’s density occurs^{55,60}.

The shape of the flare was modeled using the AGN spectrum built into CLOUDY, which consists of a multi-component continuum characterized by a rising power law with a high energy exponential cutoff and a “big blue bump” component peaking at ≈ 1 Ryd. The intensity of the flare is specified by the surface flux of hydrogen-ionizing photons, $\Phi(\text{H})$, striking the illuminated face of the cloud. The cloud distances from the Galactic center range from 2.7 to 4.1 kpc, which translates to $10^{9.25} < \Phi(\text{H}) < 10^{9.75}$ photons $\text{cm}^{-2} \text{s}^{-1}$ for an Eddington fraction $f_E = 0.3$ ^[6]. We run our models for the range $8 < \log \Phi(\text{H}) < 10$ to bracket the expected range of values⁶. Each model runs for 3.6 Myr during which the flare is on for 0.6 Myr and then is instantaneously turned off. We do not include models where the flare decays over time, because a reasonable decay time has been shown to result in only small changes when compared to an instantaneous turnoff in Magellanic stream models⁵. The combined Galactic and extragalactic radiation fields, along with the cosmic ray background are kept constant for the duration of the calculation. The models use a self-consistent approach in which the cloud is assumed to be in ionization equilibrium before the flare event occurs, thus we adopt as starting conditions the observed ion abundance, $\log n_{\text{H}}$, and cloud size ($=N_{\text{H}}/n_{\text{H}}$) from the ionization equilibrium model. After each time step of 0.2 Myr, the relative ionization fraction correction is calculated for the species of interest. A summary of these results is given in Extended Data Fig. 6.

Extended Data Fig. 7 shows the time-dependent CLOUDY results from the beginning of the Seyfert flare event ($t=0$ Myr) to current day (3.6 Myr). Since there is a large change in IC immediately after the Seyfert flare is shut off, followed by a period of relatively small variations, we plot a magnified version of the IC from 0.8–3.6 Myr as an inset panel to show these small fluctuations. After the flare is shut off (0.6 Myr), both the ICs and column densities begin to rapidly change by 0.8 Myr and stabilize by ~ 1 Myr for all sight lines.

Both sight lines approach the ICs of the equilibrium models well before 3.6 Myr. Therefore, for a Seyfert flare occurring 3.6 Myr ago with a $\log \Phi(\text{H})=8-10$ and without a long fading period, the FB HVCs have had sufficient time to reach an equilibrium ionization state and their ICs are largely unchanged by the flare.

We calculate the FB HVCs' metallicity by adding the IC calculated from $\log \Phi(\text{H})=10$ to the ion abundances calculated from Equation 3, estimating the error in IC as the difference between the ICs calculated from $\log \Phi(\text{H})$ of 8 and 10. The results are shown in Extended Data Fig. 1.

J1919-2958's and 1H1613-097's metallicity measurements made using the time-dependent ICs in Extended Data Fig. 1 have limits on their ICs due to saturation of Si III 1206 absorption, leading to lower limits on the Si III to Si II ratio. This translates to upper limits on the gas density. In Supplementary Information Section 5, we show that a 1 dex difference in Si III columns does not strongly affect the ICs or leads to nonphysical models. We therefore have removed the lower limits in Table 1 and Extended Data Fig. 1 for the metallicity measurements.

Literature Sample Ionization Corrections

We do not include LS 4825-1 or LS 4825-2 in the CLOUDY modeling described above because neither have published Si II or Si III measurements. Therefore, the clouds' gas density, derived from Si III/Si II, cannot be constrained. We instead use the grid of CLOUDY equilibrium models previously calculated in the literature for 1H1613-097 to estimate the IC for LS 4825-1's and LS 4825-2's FB HVCs¹⁷. We determine the ICs for the FB HVCs using the measured N_{HI} and a range of $\log U$ values (-3.5 , -3.0 , and -2.5), which reflect the values derived for other Milky Way halo and Fermi Bubble clouds in the literature^{17,58,61-64}. For the metallicity calculations (see Extended Data Fig. 1) we use the IC value from $\log U = -3.0$ and the other two IC values ($\log U = -3.5$ and -2.5) serve as the errors on the IC.

We also use the equilibrium CLOUDY models previously calculated for the 1H1613-097 sight line¹⁷ to estimate the ionization corrections for FB HVCs with O I detections and H I limits. For this sample we use the IC values calculated from $\log U = -3.5$ for the H I column limit as it provides an IC(O) lower limit to add to our lower-limit metallicity calculations.

We did not calculate an IC for PKS 2005-489. PKS 2005-489’s metallicity estimate, drawn from the literature, was made by comparing the FB HVC’s FUSE and STIS absorption line detections (Si II, C III, O VI, and H I Lyman series) to those of highly ionized Milky Way halo clouds with similar absorption columns and existing CLOUDY models^{33,65}.

The IC for M5-ZNG1 is calculated with the CLOUDY equilibrium modeling described above. We chose an equilibrium model because the Seyfert flare event 3.5 Myr ago was shown not to have a lasting effect on the present-day ICs in other FB HVCs. Therefore, a full time-dependent treatment was deemed unnecessary. The equilibrium IC is shown in Extended Data Fig. 1.

Data availability

The HST/COS datasets for all sources used in this paper are available in MAST with the identifier <http://dx.doi.org/10.17909/zxzh-4x54>⁶⁷, including HST Program IDs 1533, 7345, 8096, 9410, 11741, 12603, 13448, and 15339, and FUSE Program IDs A108, C149, D157, and P107. The GBT raw datasets are publicly available at the NRAO archive, <https://data.nrao.edu>; GBT programs for all sources in this paper with GBT data are GBT14B-299, GBT15B-359, GBT16B-422, GBT17B-015, GBT18A-221, GBT20A-253, and GBT20B-444. Data from GBT20B-444 will become available on the NRAO archive after the proprietary period ends July 9, 2022. Green Bank 140’ data used for calculating PG 1522+101’s HI column density limit can be requested through <https://help.nrao.edu/>. LAB data used for calculating J1509-0702’s HI column density limit is publicly available at

https://www.astro.uni-bonn.de/hisurvey/AllSky_profiles. Fully reduced data are available from the corresponding author on reasonable request.

Code availability

The IDL software used in this work is available for purchase from <https://www.13harrisgeospatial.com/Software-Technology/IDL>. The GBTIDL, VPFIT, and CLOUDY software are publicly available. The GBTIDL package for GBT data reduction and analysis can be downloaded from <https://gbtidl.nrao.edu/downloads.shtml>. The VPFIT package for fitting Voigt profiles to absorption data can be found at <https://people.ast.cam.ac.uk/~rfc/>. The CLOUDY cloud-modeling code is available at <https://gitlab.nublado.org/cloudy/cloudy/-/wikis/DownloadLinks>.

Acknowledgements

We would like to thank Joss Bland-Hawthorn for his valuable discussion on ionization from the Seyfert flare event. Support for T.A. through *HST* program 15339 was provided by NASA through grants from the Space Telescope Science Institute, which is operated by the Association of Universities for Research in Astronomy, Inc., under NASA contract NAS 5-26555. The Green Bank Observatory is a facility of the National Science Foundation, operated under a cooperative agreement by Associated Universities, Inc. The GBT data presented in this paper were obtained under Programs GBT14B-299, GBT15B-359, GBT16B-422, GBT17B-015, GBT18A-221, GBT20A-253, and GBT20B-444.

Author Contributions

T.A. led the investigation, including the sample curation, UV and radio measurements, analysis, and writing. A. J. F. led the project conceptualization and management, is the PI of the HST program that funded the research, and contributed directly to the writing of the paper. F.H.C. performed the CLOUDY modeling, contributed directly to the writing of the paper, and prepared Extended Data Fig. 7. F.J.L. reduced and analyzed the GBT data and contributed directly to the writing of the paper. R.B. provided the 1H1613-097 GBT data and its data reduction. B.P.W. provided the data reduction for the UV data. E.B.J. provided an interpretation of the cloud destruction and survival. T.K. prepared Figure 2 and Supplementary Figure 2. All authors reviewed the manuscript, contributed to the editing of the manuscript, and contributed to the discussion of the results' interpretation and implications.

Corresponding author

Correspondence to Trisha Ashley. ✉

Competing interests

The authors declare no competing interests.

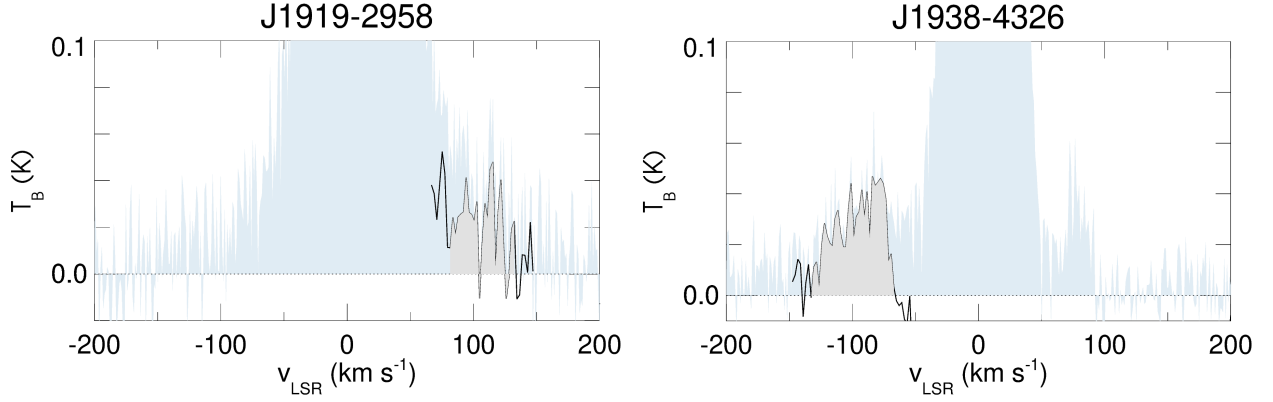
Extended Data Figures

Reference	Sight Line	v_{0UV} (km s^{-1})	X^i	$\log N_{X^i}$ (N in cm^{-2})	$\log N_{\text{HI}}$ (N in cm^{-2})	$[X^i/\text{H}]$	IC	$[X/\text{H}]$
UV and H I detections								
TW	J1919-2958	97.8 ± 7.7	O I	14.53 ± 0.04	18.30 ± 0.12	-0.46 ± 0.14	$\gtrsim -0.059 \pm 0.001$	-0.52 ± 0.14
					18.06 ± 0.13	-0.22 ± 0.14	$\gtrsim -0.048 \pm 0.001$	-0.27 ± 0.14
TW	J1938-4326	-107.1 ± 8.2	C II	13.30 ± 0.07	18.61 ± 0.38	-1.74 ± 0.39	-0.820 ± 0.010	-2.56 ± 0.39
					18.20 ± 0.29	-1.33 ± 0.30	-0.820 ± 0.010	-2.15 ± 0.30
					≤ 17.62	≥ -0.75	-0.820 ± 0.010	≥ -1.57
17	1H1613-097	-163 ± 1	O I	14.28 ± 0.03	18.23 ± 0.21	-0.64 ± 0.22	$\gtrsim -0.065 \pm 0.001$	-0.71 ± 0.22
18	LS 4825-1	92.1 ± 0.8	O I	≥ 14.39	18.36 ± 0.15	≥ -0.66	$-0.01 \pm_{-0.05}^{0.14}$	≥ -0.67
18	LS 4825-2	-78 ± 1	S II	14.57 ± 0.05	19.14 ± 0.16	0.31 ± 0.17	$-0.38 \pm_{-0.09}^{0.12}$	$-0.07 \pm_{-0.19}^{0.21}$
49	M5-ZNG1	-124 ± 7	O I	13.38 ± 0.08	16.50 ± 0.06	0.19 ± 0.11	0.31	0.50 ± 0.11
33	PKS 2005-489	168 ± 10	16.66 ± 0.83	≤ -0.70
UV detections and H I limits								
TW	J1853-4158	-120.2 ± 8.4	O I	13.70 ± 0.12	≤ 17.20	≥ -0.19	-0.04	≥ -0.23
17	J1509-0702	-115.2 ± 7.8	O I	≥ 14.61	≤ 18.10	≥ -0.18	-0.05	≥ -0.23
18	LS 4825-3	-205 ± 2	O I	13.86 ± 0.05	≤ 17.52	≥ -0.35	-0.01	≥ -0.36
18	LS 4825-4	-155 ± 1	O I	≥ 14.86	≤ 17.75	≥ 0.42	-0.01	≥ 0.41
17	PG 1522+101	-99.8 ± 8.3	O I	14.14 ± 0.10	≤ 17.92	≥ -0.47	-0.06	≥ -0.53

Extended Data Figure 1: Full Metallicity Measurements. X^i represents the UV-detected ion used for metallicity calculations and v_{0UV} is the FB HVCs' LSR velocity centroid for that ion. The ion absorption and HI emission, $\log N_{X^i}$ and N_{HI} , respectively, are listed with the HI column errors including beam smearing added in quadrature when available. We also list the ion abundances, $[X^i/\text{H}]$. The ionization correction, IC, calculations are discussed throughout the Methods section. $[X/\text{H}]$ is the corrected gas-phase elemental abundance and does not account for dust depletion. We include an OI solar abundance for M5-ZNG1's elemental abundance measurement that is updated from that in the literature^{33,54}. For a discussion of the multiple HI measurements for J1919-2958, see the Methods Section. For a discussion of dust depletion and the multiple H I measurements for J1938-4326, see Supplementary Information Section 1.

Sight line	Allowed Velocities (km s ⁻¹)	X ⁱ	UV Voigt Fit Parameters			H I Integration		H I Gaussian Fit		log N _{HI} (N in cm ⁻²)
			v _{0UV} (km s ⁻¹)	b-value (km s ⁻¹)	log N _{Xⁱ} (N in cm ⁻²)	v _{min} (km s ⁻¹)	v _{min} (km s ⁻¹)	v _{0HI} (km s ⁻¹)	FWHM (km s ⁻¹)	
J1853-4158	-49 : 0	O I	-120.2 ± 8.4	16.7 ± 5.2	13.70 ± 0.12	≤ 17.20
J1919-2958	0 : 63	O I	97.8 ± 7.7	25.9 ± 2.5	14.53 ± 0.04	82.7	133.4	18.30 ± 0.07
						107.0	133.4	18.06 ± 0.09
J1938-4326	-13 : 0	C II	-107.1 ± 8.2	24.0 ± 4.7	13.30 ± 0.07	-91.0 ± 12.4	69.4 ± 31.8	18.61 ± 0.25
						-127.4	-87.3	18.20 ± 0.04
						≤ 17.62

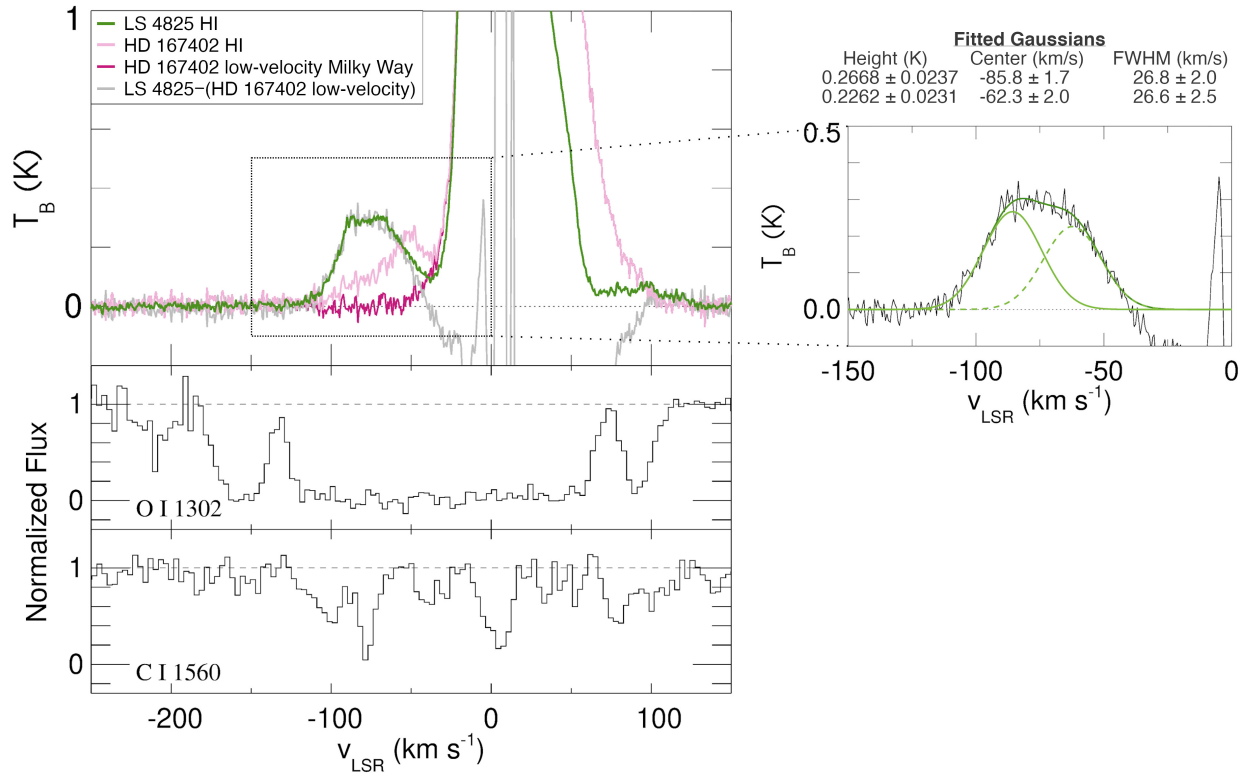
Extended Data Figure 2: UV and HI Fit Parameters for New Sight Lines. The second column represents the allowed velocity range of gas co-rotating with the Milky Way disk in each quasar’s direction⁶⁶. Xⁱ represents the ion used for metallicity calculations. The UV Voigt fit parameters of Xⁱ for each cloud are the LSR velocity centroid, v_{0UV}, the Doppler broadening parameter (b-value), and the log column density, log(N_{Xⁱ}). The UV velocity centroid errors include the 7.5 km s⁻¹ COS zero-point uncertainty. The H I Gaussian fit parameters are the LSR velocity centroid, v_{0HI}, full-width-half-max, FWHM, and log column density, log N_{HI}. For a Gaussian profile, the relation between FWHM and b-value is FWHM=1.665b. J1853-4158’s H I column was obtained using the spectrum’s rms, as described in the Methods Section. J1919-2958’s H I column was obtained by through the “flip-and-subtract” method (described in the Methods Section) using two velocity ranges for integration, which encompass all potential emission associated with the FB HVC (upper column limit) and emission least affected by stray radiation (lower column limit). J1938-4326’s H I column was obtained using a Gaussian fit to emission. Second and third measurements of the H I column were made by integrating over the C II absorber’s FWHM and then using Equation 2; see Supplementary Information Section 1 for more details.



Extended Data Figure 3: Flipped-and-subtracted GBT H I spectrum for J1919-2958 and 1938-4326. The blue shaded spectrum represents the original H I spectrum at a resolution of $\sim 1 \text{ km s}^{-1}$. The maximum velocity range used to calculate the H I column densities is shaded in grey. The black line is the flipped-and-subtracted spectra smoothed to $\sim 2 \text{ km s}^{-1}$ in the integrated velocity ranges including an additional 7 channels on each side of those velocity ranges.

Sight line	X^i	UV Voigt Fit Parameters			H I Integration		H I Gaussian Fit		$\log N_{\text{HI}}$ (N in cm^{-2})
		$v_{0 \text{ UV}}$ (km s^{-1})	b-value (km s^{-1})	$\log N_{X^i}$ (N in cm^{-2})	v_{min} (km s^{-1})	v_{min} (km s^{-1})	$v_{0 \text{ HI}}$ (km s^{-1})	FWHM (km s^{-1})	
1H1613-097	O I	-163 ± 1	17.6 ± 1.7	14.28 ± 0.03	172.2 ± 0.1	12.8 ± 0.8	18.23 ± 0.03
LS 4825-1	O I	92.1 ± 0.8	11.9 ± 2.5	≥ 14.39	82.0	101.9	18.36 ± 0.01
LS 4825-2	S II	-78 ± 1	6.9 ± 0.6	14.57 ± 0.05	-85.8 ± 1.7	26.8 ± 2.0	19.14 ± 0.05
LS 4825-3	O I	-205 ± 2	18.6 ± 2.5	13.86 ± 0.05	-221.1	-190.3	≤ 17.52
LS 4825-4	O I	-155 ± 1	14.2 ± 0.5	≥ 14.86	-167.4	-143.2	≤ 17.75
M5-ZNG1	O I	-124 ± 7	...	13.38 ± 0.08	16.50 ± 0.06
J1509-0702	O I	-115.2 ± 7.8	9.6 ± 5.1	≥ 14.61	≤ 18.10
PG 1522+101	O I	-99.8 ± 8.3	12.7 ± 6.3	14.14 ± 0.10	≤ 17.92
PKS 2005-489	...	168 ± 10	16.66 ± 0.83

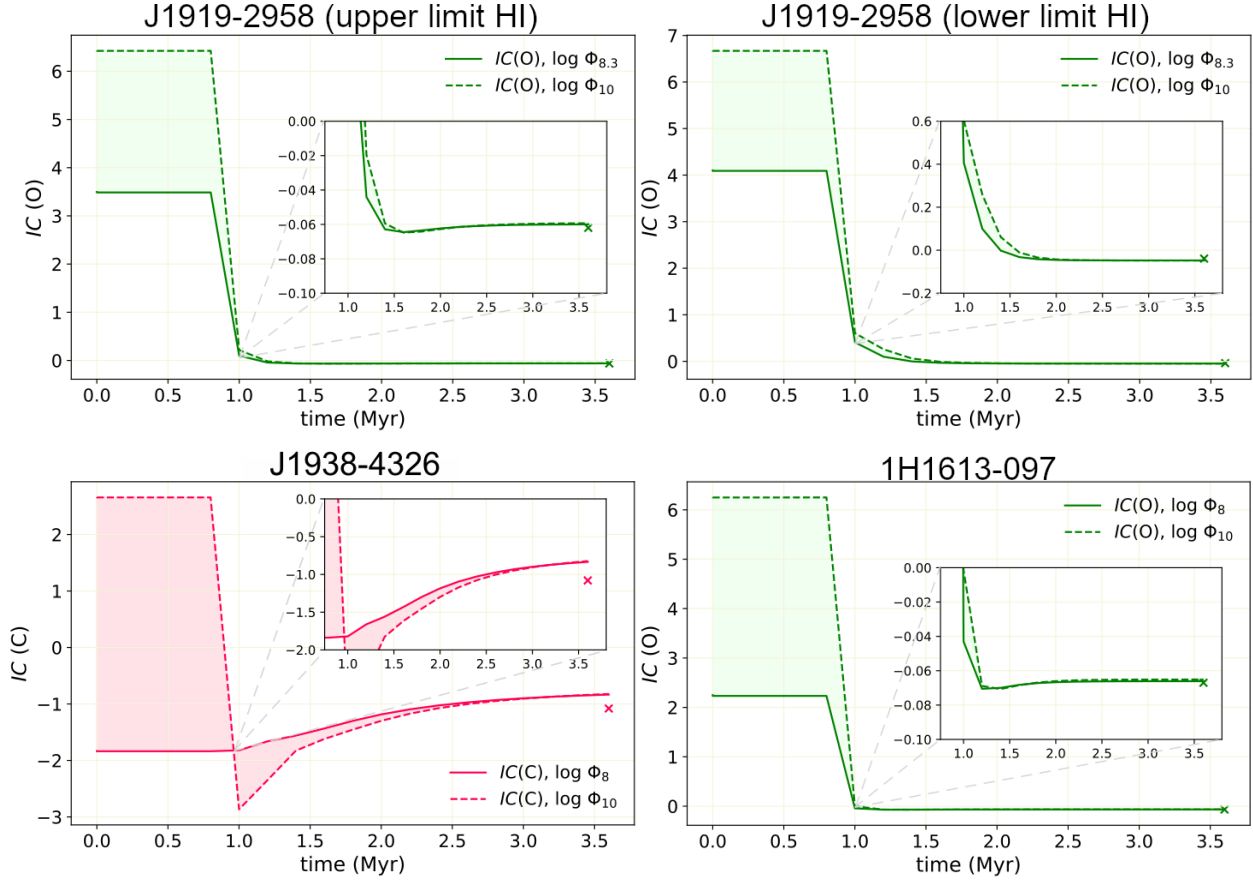
Extended Data Figure 4: UV and H I Fit Parameters for Literature Sight Lines. This table lists UV and H I fit parameters for the literature FB HVCs, similar to that done for the new sight lines in Supplementary Table 2. M5-ZNG1 has a literature H I measurement based on a combination of FUSE profile fitting and curve-of-growth measurements⁴⁹. J1509-0702 and PG 1522+10 have H I measurements based on their average rms of emission-free channels (rms of 0.055 and 0.032 K, respectively). PKS 2005-489's $\log N_{\text{HI}}$ is from Lyman series measurements in the literature³³.



Extended Figure 5: Deconvolution of LS 4825’s H I spectrum. Left: LS 4825’s and HD 167402’s H I spectra plotted against HD 167402’s low-velocity Milky Way component and LS 4825’s residual “ I spectrum after subtracting HD 167402’s low-velocity Milky Way component. We also plot LS4825’s O I λ 1302 and C I λ 1560 spectrum for comparison. Right: The individual and combined Gaussian fits to LS 4825’s residual negative-velocity components.

Sight line	X^i	$v_{0\text{ UV}}$ (km s^{-1})	[Si III/Si II]	log U Eq.	log n_{H} (n in cm^{-3})	log N_{H} (N in cm^{-2})	Depth (pc)	IC(X^i) Eq.	IC(X^i) $\Phi(\text{H})_8$	IC(X^i) $\Phi(\text{H})_{10}$
J1919-2958	O I	97.8 ± 7.7	≥ -0.37	max H I: $\gtrsim -3.47$ min H I: $\gtrsim -3.23$	≤ -0.57 ≤ -0.82	19.52 19.66	≥ 41 ≥ 96	$\gtrsim -0.062$ $\gtrsim -0.039$	$\gtrsim -0.060$ $\gtrsim -0.047$	$\gtrsim -0.059$ $\gtrsim -0.048$
1H1613-097	O I	-163 ± 1	≥ -0.45	$\gtrsim -3.70$	≤ -0.35	19.34	≥ 16	$\gtrsim -0.067$	$\gtrsim -0.066$	$\gtrsim -0.065$
J1938-4326	C II	-107.1 ± 8.2	-0.67	-3.11	-0.94	20.02	298	-1.08	-0.830	-0.820

Extended Data Figure 6: X^i represents the ion used for the metallicity calculations and $v_{0\text{ UV}}$ is the UV velocity centroid of each component. The logarithmic Si III to Si II ion ratio, [Si III /Si II], is calculated using the column densities measured in previous Fermi Bubble UV Surveys^{17,20}; for J1938-4326 we use the [Si III /C II] ratio. U is the ionization parameter, equal to the ratio of the ionizing photon density to the gas density. The log hydrogen number density and column density of the clouds are given as log n_{H} and log N_{H} , respectively. The depth is the calculated size of the cloud along the line-of-sight. The present day ionization corrections are given as IC(X^i) Eq. for the equilibrium models, and IC(X^i) $\Phi(\text{H})_8$ and IC(X^i) $\Phi(\text{H})_{10}$ for the time-dependent models at two ionizing photon fluxes, log $\Phi(\text{H})=8$ and 10, respectively.



Extended Data Figure 7: Time-dependent ionization corrections versus time calculated from our CLOUDY models. The results are given for two ionizing fluxes: $\log \Phi(\text{H}) = 8$ (solid line) and 10 (dashed line), where $\Phi(\text{H})$ has units of photons $\text{cm}^{-2} \text{s}^{-1}$ and where colored shading shows intermediate ionizing fluxes. Each panel shows the ionization correction across the full time interval modeled (0–3.6 Myr), with an inset plot magnifying the flatter part of the curves after the initial flash to emphasize the late-time behavior. The equilibrium results are marked with an ‘x’ at 3.6 Myr in each panel.

References

- [1] Guo, F. & Mathews, W. G. The Fermi Bubbles. I. possible evidence for recent agn jet activity in the Galaxy. *The Astrophysical Journal* **756**, 181 (2012). URL <https://doi.org/10.1088/0004-637x/756/2/181>.
- [2] Mou, G., Yuan, F., Bu, D., Sun, M. & Su, M. Fermi Bubbles inflated by winds launched from the hot accretion flow in SGR A*. *The Astrophysical Journal* **790**, 109 (2014). URL <https://doi.org/10.1088/0004-637x/790/2/109>.
- [3] Miller, M. J. & Bregman, J. N. The interaction of the Fermi Bubbles with the Milky Way's hot gas halo. *The Astrophysical Journal* **829**, 9 (2016). URL <https://doi.org/10.3847/0004-637x/829/1/9>.
- [4] Predehl, P., Sunyaev, R. & Becker, W. Detection of large-scale X-ray bubbles in the Milky Way halo. *Nature* **588**, 227–231 (2020). URL <https://doi.org/10.1038/s41586-020-2979-0>.
- [5] Bland-Hawthorn, J., Maloney, P. R., Sutherland, R. S. & Madsen, G. J. Fossil imprint of a powerful flare at the Galactic center along the Magellanic stream. *The Astrophysical Journal* **778**, 58 (2013). URL <https://doi.org/10.1088/0004-637x/778/1/58>.
- [6] Bland-Hawthorn, J. *et al.* The large-scale ionization cones in the Galaxy. *The Astrophysical Journal* **886**, 45 (2019). URL <https://doi.org/10.3847/1538-4357/ab44c8>.
- [7] Fox, A. J. *et al.* Kinematics of the Magellanic Stream and implications for its ionization. *The Astrophysical Journal* **897**, 23 (2020). URL <https://doi.org/10.3847/1538-4357/ab92a3>.
- [8] Crocker, R. M., Bicknell, G. V., Taylor, A. M. & Carretti, E. A unified model of the Fermi Bubbles, microwave haze, and polarized radio lobes: Reverse shocks in the

- Galactic center's giant outflows. *The Astrophysical Journal* **808**, 107 (2015). URL <https://doi.org/10.1088/0004-637x/808/2/107>.
- [9] Sarkar, K. C., Nath, B. B. & Sharma, P. Multiwavelength features of Fermi Bubbles as signatures of a Galactic wind. *Monthly Notices of the Royal Astronomical Society* **453**, 3827–3838 (2015). URL <https://doi.org/10.1093/mnras/stv1806>.
- [10] Su, M., Slatyer, T. R. & Finkbeiner, D. P. Giant gamma-ray bubbles from FERMI-LAT: active galactic nucleus activity or bipolar galactic wind? *The Astrophysical Journal* **724**, 1044–1082 (2010). URL <https://doi.org/10.1088/0004-637x/724/2/1044>.
- [11] Dobler, G., Finkbeiner, D. P., Cholis, I., Slatyer, T. & Weiner, N. The Fermi haze: a gamma-ray counterpart to the microwave haze. *The Astrophysical Journal* **717**, 825–842 (2010). URL <https://doi.org/10.1088/0004-637x/717/2/825>.
- [12] Ackermann, M. *et al.* The spectrum and morphology of the Fermi Bubbles. *The Astrophysical Journal* **793**, 64 (2014). URL <https://doi.org/10.1088/0004-637x/793/1/64>.
- [13] Bland-Hawthorn, J. & Cohen, M. The large-scale bipolar wind in the galactic center. *The Astrophysical Journal* **582**, 246–256 (2003). URL <https://doi.org/10.1086/344573>.
- [14] Dobler, G. & Finkbeiner, D. P. Extended anomalous foreground emission in the WMAP three-year data. *The Astrophysical Journal* **680**, 1222–1234 (2008). URL <https://doi.org/10.1086/587862>.
- [15] Carretti, E. *et al.* Giant magnetized outflows from the centre of the Milky Way. *Nature* **493**, 66 EP – (2013). URL <https://doi.org/10.1038/Natureure11734>.

- [16] Fox, A. J. *et al.* Probing the Fermi Bubbles in ultraviolet absorption: a spectroscopic signature of the Milky Way's biconical nuclear outflow. *The Astrophysical Journal* **799**, L7 (2015). URL <https://doi.org/10.1088/2041-8205/799/1/17>.
- [17] Bordoloi, R. *et al.* Mapping the nuclear outflow of the Milky Way: studying the kinematics and spatial extent of the northern Fermi Bubble. *The Astrophysical Journal* **834**, 191 (2017). URL <https://doi.org/10.3847/1538-4357/834/2/191>.
- [18] Savage, B. D. *et al.* Probing the outflowing multiphase gas ~ 1 kpc below the Galactic center. *The Astrophysical Journals* **232**, 25 (2017). URL <https://doi.org/10.3847/1538-4365/aa8f4c>.
- [19] Karim, M. T. *et al.* Probing the southern Fermi Bubble in ultraviolet absorption using distant AGNs. *The Astrophysical Journal* **860**, 98 (2018). URL <https://doi.org/10.3847/1538-4357/aac167>.
- [20] Ashley, T. *et al.* Mapping outflowing gas in the Fermi Bubbles: A UV absorption survey of the Galactic nuclear wind. *The Astrophysical Journal* **898**, 128 (2020). URL <https://doi.org/10.3847/1538-4357/ab9ff8>.
- [21] McClure-Griffiths, N. M. *et al.* Atomic hydrogen in a galactic center outflow. *The Astrophysical Journal* **770**, L4 (2013). URL <https://doi.org/10.1088/2041-8205/770/1/14>.
- [22] Di Teodoro, E. M. *et al.* Blowing in the Milky Way wind: Neutral hydrogen clouds tracing the Galactic nuclear outflow. *The Astrophysical Journal* **855**, 33 (2018). URL <https://doi.org/10.3847/1538-4357/aaad6a>.
- [23] Lockman, F. J., Di Teodoro, E. M. & McClure-Griffiths, N. M. Observation of acceleration of HI clouds within the fermi bubbles. *The Astrophysical Journal* **888**, 51 (2020). URL <https://doi.org/10.3847/1538-4357/ab55d8>.

- [24] Di Teodoro, E. M., McClure-Griffiths, N. M., Lockman, F. J. & Armillotta, L. Cold gas in the Milky Way’s nuclear wind. *Nature* **584**, 364–367 (2020). URL <https://doi.org/10.1038/s41586-020-2595-z>.
- [25] Lockman, F. J. & McClure-Griffiths, N. M. Tracing the Milky Way nuclear wind with 21 cm atomic hydrogen emission. *The Astrophysical Journal* **826**, 215 (2016). URL <https://doi.org/10.3847/0004-637x/826/2/215>.
- [26] McCourt, M., O’Leary, R. M., Madigan, A.-M. & Quataert, E. Magnetized gas clouds can survive acceleration by a hot wind. *Monthly Notices of the Royal Astronomical Society* **449**, 2–7 (2015). URL <https://doi.org/10.1093/mnras/stv355>.
- [27] Scannapieco, E. & Brüggén, M. The launching of cold clouds by galaxy outflows. I. hydrodynamic interactions with radiative cooling. *The Astrophysical Journal* **805**, 158 (2015). URL <https://doi.org/10.1088/0004-637x/805/2/158>.
- [28] Schneider, E. E. & Robertson, B. E. Hydrodynamical coupling of mass and momentum in multiphase galactic winds. *The Astrophysical Journal* **834**, 144 (2017). URL <https://doi.org/10.3847/1538-4357/834/2/144>.
- [29] Zhang, D., Thompson, T. A., Quataert, E. & Murray, N. Entrainment in trouble: cool cloud acceleration and destruction in hot supernova-driven galactic winds. *Monthly Notices of the Royal Astronomical Society* **468**, 4801–4814 (2017). URL <https://doi.org/10.1093/mnras/stx822>.
- [30] Wakker, B. P. *et al.* Accretion of low-metallicity gas by the Milky Way. *Nature* **402**, 388–390 (1999). URL <https://doi.org/10.1038/46498>.
- [31] Richter, P. *et al.* The diversity of high- and intermediate-velocity clouds: Complex C versus IV Arch. *The Astrophysical Journal* **559**, 318–325 (2001). URL <https://doi.org/10.1086/322401>.

- [32] Fox, A. J. *et al.* Highly ionized gas surrounding high-velocity cloud Complex C. *The Astrophysical Journal* **602**, 738–759 (2004). URL <https://doi.org/10.1086/381024>.
- [33] Keeney, B. A. *et al.* Does the Milky Way produce a nuclear galactic wind? *The Astrophysical Journal* **646**, 951–964 (2006). URL <https://doi.org/10.1086/505128>.
- [34] Jenkins, E. B. A unified representation of gas-phase element depletions in the interstellar medium. *The Astrophysical Journal* **700**, 1299–1348 (2009). URL <https://doi.org/10.1088/0004-637x/700/2/1299>.
- [35] Savage, B. D. & Sembach, K. R. Interstellar abundances from absorption-line observations with the Hubble Space Telescope. *Annual Review of Astronomy and Astrophysics* **34**, 279–329 (1996). URL <https://doi.org/10.1146/annurev.astro.34.1.279>.
- [36] Kataoka, J. *et al.* SUZAKU observations of the diffuse x-ray emission across the Fermi Bubbles' edges. *The Astrophysical Journal* **779**, 57 (2013). URL <https://doi.org/10.1088/0004-637x/779/1/57>.
- [37] Afflerbach, A., Churchwell, E. & Werner, M. W. Galactic abundance gradients from infrared fine-structure lines in compact HII regions. *The Astrophysical Journal* **478**, 190–205 (1997). URL <https://doi.org/10.1086/303771>.
- [38] Rolleston, W. R. J., Smartt, S. J., Dufton, P. L. & Ryans, R. S. I. The Galactic metallicity gradient. *Astronomy and Astrophysics* **363**, 537–554 (2000).
- [39] Gritton, J. A., Shelton, R. L. & Kwak, K. Mixing between high velocity clouds and the Galactic halo. *The Astrophysical Journal* **795**, 99 (2014). URL <https://doi.org/10.1088/0004-637x/795/1/99>.

- [40] Gronke, M. & Oh, S. P. The growth and entrainment of cold gas in a hot wind. *Monthly Notices of the Royal Astronomical Society: Letters* **480**, L111–L115 (2018). URL <https://academic.oup.com/mnrasl/article-pdf/480/1/L111/25447461/sly131.pdf>.
- [41] Miller, M. J., Hodges-Kluck, E. J. & Bregman, J. N. The Milky Way’s hot gas kinematics: signatures in current and future O VII absorption line observations. *The Astrophysical Journal* **818**, 112 (2016). URL <https://doi.org/10.3847/0004-637x/818/2/112>.
- [42] Henley, D. B., Gritton, J. A. & Shelton, R. L. The effect of mixing on the observed metallicity of the Smith Cloud. *The Astrophysical Journal* **837**, 82 (2017). URL <https://doi.org/10.3847/1538-4357/aa5df7>.
- [43] Armillotta, L., Fraternali, F. & Marinacci, F. Efficiency of gas cooling and accretion at the disc–corona interface. *Monthly Notices of the Royal Astronomical Society* **462**, 4157–4170 (2016). URL <https://doi.org/10.1093/mnras/stw1930>.
- [44] Marasco, A., Fraternali, F. & Binney, J. J. Supernova-driven gas accretion in the Milky Way. *Monthly Notices of the Royal Astronomical Society* **419**, 1107–1120 (2011). URL <https://doi.org/10.1111/j.1365-2966.2011.19771.x>.
- [45] Schneider, E. E., Ostriker, E. C., Robertson, B. E. & Thompson, T. A. The physical nature of starburst-driven galactic outflows. *The Astrophysical Journal* **895**, 43 (2020). URL <https://doi.org/10.3847/1538-4357/ab8ae8>.
- [46] Birnboim, Y. & Dekel, A. Virial shocks in galactic haloes? *Monthly Notices of the Royal Astronomical Society* **345**, 349–364 (2003). URL <https://doi.org/10.1046/j.1365-8711.2003.06955.x>.
- [47] Cattaneo, A. & Teyssier, R. AGN self-regulation in cooling flow clusters. *Monthly Notices of the Royal Astronomical Society* **376**, 1547–1556 (2007). URL <https://doi.org/10.1111/j.1365-2966.2007.11512.x>.

- [48] Beckmann, R. S. *et al.* Cosmic evolution of stellar quenching by AGN feedback: clues from the Horizon-AGN simulation. *Monthly Notices of the Royal Astronomical Society* **472**, 949–965 (2017). URL <https://doi.org/10.1093/mnras/stx1831>.
- [49] Zech, W. F., Lehner, N., Howk, J. C., Dixon, W. V. D. & Brown, T. M. The high-velocity gas toward Messier 5: Tracing feedback flows in the inner Galaxy. *The Astrophysical Journal* **679**, 460–480 (2008). URL <https://doi.org/10.1086/587135>.
- [50] Monroe, T. R. *et al.* THE UV-Bright Quasar Survey (UVQS): DR1. *AJ* **152**, 25 (2016). URL <https://doi.org/10.3847/0004-6256/152/1/25>.
- [51] Boothroyd, A. I. *et al.* Accurate Galactic 21-cm H I measurements with the NRAO Green Bank Telescope. *Astronomy and Astrophysics* **536**, A81 (2011). URL <https://doi.org/10.1051/0004-6361/201117656>.
- [52] Fox, A. J. *et al.* Chemical abundances in the Leading Arm of the Magellanic Stream. *The Astrophysical Journal* **854**, 142 (2018). URL <https://doi.org/10.3847/1538-4357/aaa9bb>.
- [53] Kalberla, P. M. W. *et al.* The Leiden/Argentine/Bonn (LAB) survey of Galactic HI - final data release of the combined LDS and IAR surveys with improved stray-radiation corrections. *A&A* **440**, 775–782 (2005). URL <https://doi.org/10.1051/0004-6361:20041864>.
- [54] Asplund, M., Grevesse, N., Sauval, A. J. & Scott, P. The chemical composition of the Sun. *Annual Review of Astronomy and Astrophysics* **47**, 481–522 (2009). URL <https://doi.org/10.1146/annurev.astro.46.060407.145222>.
- [55] Ferland, G. J. *et al.* The 2017 release Cloudy. *Revista Mexicana de Astronomia y Astrofisica* **53**, 385–438 (2017). URL <https://ui.adsabs.harvard.edu/abs/2017RMxAA..53..385F>.

- [56] Bland-Hawthorn, J. & Maloney, P. R. The escape of ionizing photons from the Galaxy. *The Astrophysical Journal* **510**, L33–L36 (1999). URL <https://doi.org/10.1086/311797>.
- [57] Fox, A. J. *et al.* Multiphase high-velocity clouds toward HE 0226-4110 and PG 0953+414. *The Astrophysical Journal* **630**, 332–354 (2005). URL <https://doi.org/10.1086/431915>.
- [58] Fox, A. J. *et al.* The COS/UVES absorption survey of the Magellanic stream. III. ionization, total mass, and inflow rate onto the Milky Way. *The Astrophysical Journal* **787**, 147 (2014). URL <https://doi.org/10.1088/0004-637x/787/2/147>.
- [59] Indriolo, N., Geballe, T. R., Oka, T. & McCall, B. J. H^+_{3} in diffuse interstellar clouds: a tracer for the cosmic-ray ionization rate. *The Astrophysical Journal* **671**, 1736–1747 (2007). URL <https://doi.org/10.1086/523036>.
- [60] Chatzikos, M. *et al.* Implications of coronal line emission in NGC 4696*. *Monthly Notices of the Royal Astronomical Society* **446**, 1234–1244 (2015). URL <https://doi.org/10.1093/mnras/stu2173>.
- [61] Collins, J. A., Shull, J. M. & Giroux, M. L. Highly ionized high-velocity clouds: Hot intergalactic medium or Galactic halo? *The Astrophysical Journal* **623**, 196–212 (2005). URL <https://doi.org/10.1086/428566>.
- [62] Richter, P., Charlton, J. C., Fangano, A. P. M., Bekhti, N. B. & Masiero, J. R. A population of weak metal-line absorbers surrounding the Milky Way. *The Astrophysical Journal* **695**, 1631–1647 (2009). URL <https://doi.org/10.1088/0004-637x/695/2/1631>.

- [63] Tripp, T. M. *et al.* The hidden mass and large spatial extent of a post-starburst galaxy outflow. *Science* **334**, 952–955 (2011). URL <https://science.sciencemag.org/content/334/6058/952.full.pdf>.
- [64] Fox, A. J. *et al.* On the metallicity and origin of the Smith high-velocity cloud. *The Astrophysical Journal* **816**, L11 (2016). URL <https://doi.org/10.3847/2041-8205/816/1/L11>.
- [65] Collins, J. A., Shull, J. M. & Giroux, M. L. Highly ionized high-velocity clouds toward PKS 2155-304 and Markarian 509. *The Astrophysical Journal* **605**, 216–229 (2004). URL <https://doi.org/10.1086/382269>.
- [66] Wakker, B. P. Distribution and origin of high-velocity clouds. II. statistical analysis of the whole-sky survey. *Astronomy and Astrophysics* **250**, 499 (1991). URL <https://ui.adsabs.harvard.edu/abs/1991A&A...250..499W>.
- [67] Ashley, T., Data for diverse metallicities of Fermi Bubble Clouds.... *MAST*. 10.17909/zxzh-4x54 (2022).

Supplementary Information to Diverse Metallicities of Fermi Bubble Clouds Indicate Dual Origins in the Disk and Halo

1 Dust depletion and J1938-4326's low metallicity

Dust depletion does not strongly affect oxygen measurements and is largely thought to not strongly affect sulfur measurements^{34,35}. However, dust depletion can be significant for carbon, which is used to measure the metallicity for J1938-4326. Without taking into account dust depletion affects, the log of J1938-4326's gas-phase elemental abundance is 0.28% solar (see Extended Data Fig. 1). In the densest clouds, carbon levels can be depleted by up to -0.58 dex^{34,68}. That would raise the metallicity of the FB HVC towards J1938-4326 to 1% solar (or -1.98 dex in log space), a resolutely low metallicity.

With such a low metallicity, we also explore the possibility that the H I spectrum towards J1938-4326 may have emission from multiple clouds contributing to the H I Gaussian fit shown in Figure 2, which may not all be associated with the FB HVC towards J1938-4326. To do this, we integrate the H I emission over the velocity range of the C II absorption's FWHM and centered on the C II absorption's v_{0UV} (-127 to -87 km s⁻¹). This results in a $\log N_{\text{HI}} = 18.20$. Assuming the same IC as listed in Extended Data Fig. 1 and a dust depletion of -0.58 dex, the resulting metallicity would still only reach 2.7% solar. If we instead assume that none of the H I detected in this velocity range is associated with the FB HVC and use Equation 2 to estimate an upper limit on the H I column density, then we measure $\log N_{\text{HI}} \leq 17.62$; assuming the same IC and dust depletion, the metallicity is raised to only 10% solar. Therefore, the data indicate that this FB HVC has a low metallicity even when dust depletion is taken into account. In Table 1 we include J1938-4326's metallicity as

a range between that which is calculated using the Gaussian fit to the H I and that which is calculated using Equation 2; both limits contain a dust depletion level of -0.58 dex. We also include the various H I column measurements in Extended Data Fig. 1 and 2.

2 Check of J1938-4326’s HI Gaussian fit

To verify the Gaussian-fit H I column density measurement of J1938-4326 in Extended Data Fig. 2, we use the same flip-and-subtract measurement method that is used to determine J1919-2958’s H I column. The remaining “flipped-and-subtracted” spectra is shown in Extended Data Fig. 3. We integrate the emission from -131.7 to -67.2 km s $^{-1}$ and calculate a $\log N_{\text{HI}}$ of 18.53 ± 0.04 using Equation 1; this $\log N_{\text{HI}}$ from the flip-and-subtract method is within the errors of that listed in Extended Data Fig. 2. If we instead use the FWHM and velocity centroid of J1938-4326’s C II absorption to integrate over the residual spectrum (-127.4 to -87.3 km s $^{-1}$), then the $\log N_{\text{HI}}$ decreases by 0.21 dex or 0.04 dex below that of column minus the error listed in Extended Data Fig. 2.

3 Effects of the XX-polarization on GBT maps

All XX-polarization data has been discarded in the GBT H I emission maps presented in Figure 1 due to spurious features at levels of tens of mK produced by frequency switching. Typically these features can be ignored due to their low levels; however, H I emission of the FB HVCs in this work also appear on the level of 10-20 mK (see Supplementary Fig. 1), making it possible to misinterpret these spurious features as emission. The YY polarization only suffers minor spurious waves that are not likely to be misinterpreted as emission. An example of the difference between the YY-only and XX-YY combined spectra from the GBT maps is shown in Supplementary Fig. 1. In the single-pointing H I data near the emission

velocity regions these spurious features were not as pronounced; therefore, we left the XX-polarization in the single-pointing data to obtain the better signal-to-noise for the column density measurements presented in Extended Data Fig. 2.

4 CLOUDY model comparison for J1919-2958's range of HI columns

Because of the range in J1919-2958's H I column density, we run two sets of CLOUDY models for this sight line. CLOUDY produces a list of predicted ion columns for each model. In the equilibrium models of both the lower and upper H I column limit, we compared the FB HVC's measured ion columns to CLOUDY's predicted columns (for Al II λ 1670, C II λ 1334, C IV λ 1548, 1550, Fe II λ 1144, 1608, O I λ 1302, S II λ 1250, 1253, 1259, Si II λ 1190, 1193, 1260, 1526, Si III λ 1206, and Si IV λ 1393, 1402). We find that of the two CLOUDY models, the upper H I column density limit model more closely coincides with the measured column densities. The average absolute relative errors in the linear column densities are 2.2 and 0.87 for the lower and upper H I column density limits, respectively. Therefore, the CLOUDY models slightly favor the upper H I column density limit and lower metallicity for the FB HVC toward J1919-2958.

5 Ionization correction dependence on saturation of Si III

J1919-2958's and 1H1613-097's ICs in Extended Data Fig. 1 are limits due to saturation of Si III 1206 absorption, resulting in upper limits on the gas density. However, IC(O) values tend to be near zero for $\log N_{\text{HI}} > 18.5^{[17]}$. We therefore test the robustness of these metallicity

measurements by changing the saturated $\log N_{\text{Si III}}$ measurement by 1 dex and recalculating the metallicities using the ionization equilibrium models. We show the model parameters and results in Supplementary Table 2. The metallicity measurements for 1H1613-097 and J1919-2958's upper H I column density limit from a 1 dex increase in Si III columns are approximately within the metallicity errors listed in Extended Data Fig. 1. This 1 dex increase shows that the metallicity results are not strongly dependent on Si III saturation for high H I columns. Conversely, J1919-2958's lower H I column density limit ($\log N_{\text{HI}}=18.06$) does have a significant change in IC of about -0.41 dex when the Si III measurement increases by 1 dex. We note, however, that J1919-2958's lower limit H I column model results for the increase in 1 dex give an unrealistic cloud depth of ~ 6 kpc. Additionally, the CLOUDY model with $\log N_{\text{Si III}}=13.71$ has predicted ion columns significantly closer to the measured columns, with an average absolute relative error on the linear ion columns of 2.2, whereas the model with $\log N_{\text{Si III}}=14.71$ has an average absolute relative error of 25. We therefore remove the metallicity measurements' lower limits in Table 1 and Extended Data Fig. 1.

6 Supplementary tables

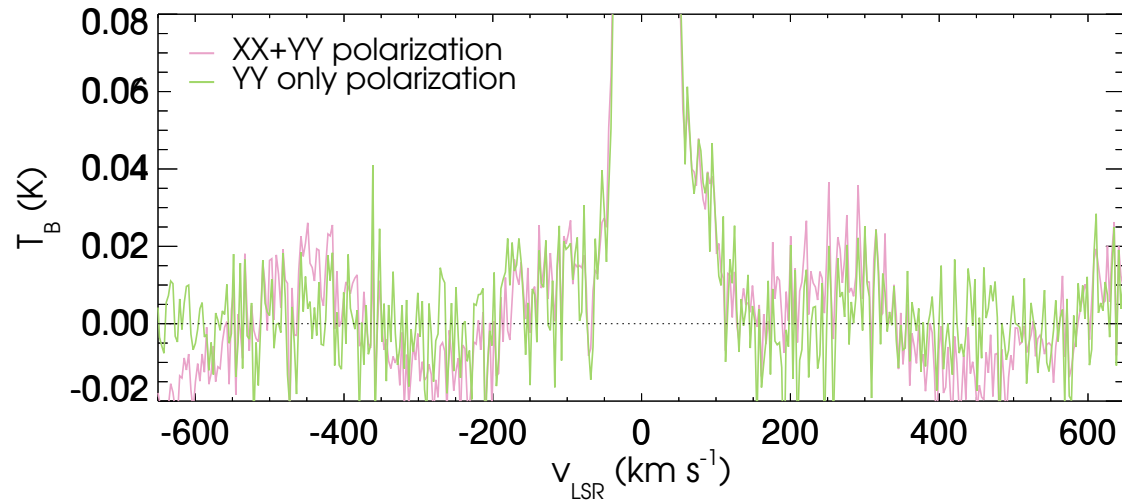
Sight line	$\sigma_{v_{0\text{HI}}}$ (km s ⁻¹)	σ_{FWHM} (km s ⁻¹)	ϵ_{Beam} (dex)
J1919-2958	1.3	5.2	0.10
J1938-4326	6.7	7.7	0.29
1H1613-097	0.61	0.74	0.21

Supplementary Table 1: Beam Smearing Estimates. This table quantifies the beam smearing uncertainties of our H I measurements. The standard deviations of the H I velocity centroid and FWHM are given as $\sigma_{v_{0\text{HI}}}$ and σ_{FWHM} , respectively, measured by comparing pointings along the central quasar sight line with those centered a half beamwidth away. ϵ_{Beam} is the beam-smearing error on the H I column density.

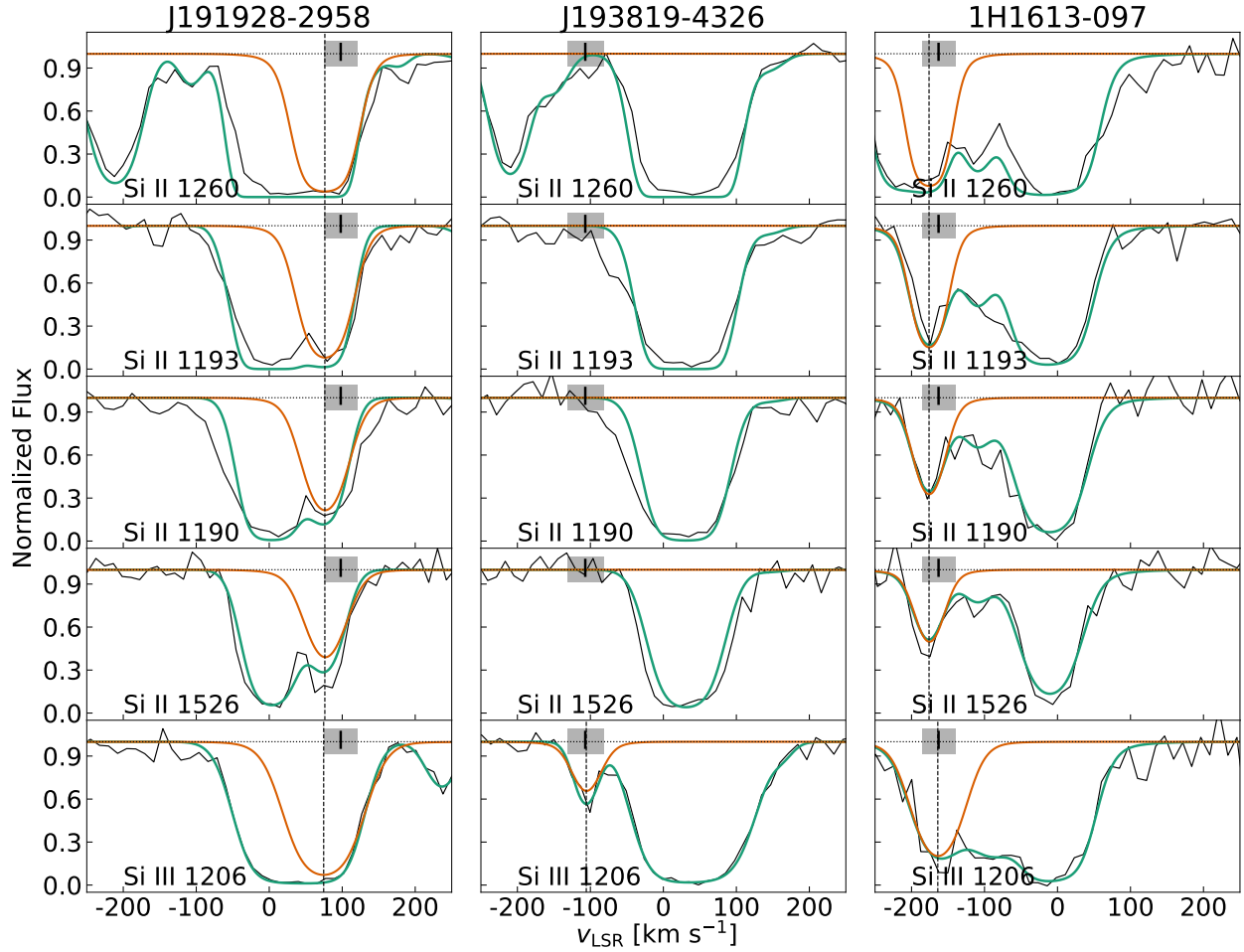
Sight line	$\log N_{\text{Si III}}$	[Si III/Si II]	$\log n_{\text{H}}$ (n in cm ⁻³)	Depth (pc)	IC(O) Eq.	Z (Z_{\odot})	
J1919-2958	max H I:	Measured: 13.71	-0.37	-0.57	41	-0.062	0.30
		+1 dex: 14.71	0.63	-1.57	4100	0.132	0.47
	min H I:	Measured: 13.71	-0.37	-0.82	96	-0.039	0.54
		+1 dex: 14.71	0.63	-1.70	6100	0.367	1.4
1H1613-097		Measured: 13.38	-0.45	-0.35	16	-0.067	0.19
		+1 dex: 14.38	0.55	-1.33	1400	0.064	0.26

Supplementary Table 2: For each absorber we calculate the effect on IC(O) from a 1 dex increase in $\log N_{\text{Si III}}$. This table demonstrates the marginal effect of different degrees of saturation in Si III 1206 on most oxygen ionization corrections. Only the minimum H I measurements for J1919-2958 show a significant change in metallicity; however, the model produces unrealistic cloud depths and ion columns that have high average absolute relative errors on the ion column densities.

7 Supplementary figures



Supplementary Figure 1: Spectra from J1919-2958 GBT H I maps comparing both polarizations combined (XX+YY; pink) and only the YY-polarization (green). This figure demonstrates that the spurious spectral features in the maps are prominent in the XX-polarization.



Supplementary Figure 2: Profiles of the Si II and Si III absorption lines for J1919-2958, J1938-4326, and 1H1613-098. The black tick marks and grey bars at the top of every panel represents the velocity centroid and three times its error of the O I (we include a COS zero-velocity offset in the v_{0UV} for 1H1613-097, which is not reported in the literature table from which the velocity centroid was drawn¹⁷). The Voigt-profile fits to the Si II and Si III absorption are denoted by the orange lines when detected and the full fit to each absorption spectra is given by the green line. The velocity centroids of the Si II and Si III fits are marked with a dashed vertical line.

Supplementary information references

68. Sofia, U. J., Parvathi, V. S., Babu, B. R. S. & Murthy, J. Determining interstellar carbon abundances from strong-line transitions. *Astron. J.* **141**, 22, (2011).